In-Situ Nanoindentation Surface Topography of Lead-Free Piezoelectric Thin Films

Maxence Bigerelle, Julie Lemesle, Alex Montagne, Denis Remiens

applied sciences

MDPI

Article

In-Situ Nanoindentation Surface Topography of Lead-Free Piezoelectric Thin Films

Maxence Bigerelle [1,*], Julie Lemesle [2,3], Alex Montagne [1] and Denis Remiens [4]

[1] CNRS UMR 8201–LAMIH—Laboratoire d'Automatique, de Mécanique et d'Informatique Industrielles et Humaines, University Polytechnique Hauts-de-France, 59313 Valenciennes, France; alex.montagne@uphf.fr
[2] Valutec, University Polytechnique Hauts-de-France, 59314 Valenciennes, France; julie.lemesle@uphf.fr
[3] U.R Concept, 59300 Valenciennes, France
[4] CNRS UMR 8520–IEMN—Institut d'Electronique, de Microélectronique et de Nanotechnologie, University Polytechnique Hauts-de-France, 59309 Valenciennes, France; denis.remiens@uphf.fr
* Correspondence: maxence.bigerelle@uphf.fr

Abstract: Surface roughness significantly affects the performance of microelectromechanical systems (MEMS) and piezoelectric films. This study investigates the impact of surface roughness on the mechanical properties of thin piezoelectric films using nanoindentation and scanning probe microscopy (SPM). Four piezoelectric films with different thicknesses (220, 350, and 450 nm) and substrate configurations (LNO/SiO_2/Si or LNO/Si) were analyzed. A discriminant analysis revealed that the fractal dimension is more effective than the arithmetic mean height (Sa) for distinguishing surfaces, with only 2% misclassification versus 25% for Sa. A multiscale analysis identified the Smr2 parameter with low-pass filtering at 140 nm as highly effective for surface discrimination, achieving only 0.1% misclassification. The analysis of the roughness parameter Sa at various scales showed that band-pass filtering at 500 nm yielded a 0.7% misclassification rate, indicating its relevance for fractal roughness characterization. Most relevant roughness parameters for mechanical property correlation were found: Smr2 with low-pass filtering at 500 nm correlated best with hardness (R^2 = 0.82), and Vvc with low-pass filtering at 2 nm correlated best with reduced elastic modulus (R^2 = 0.84). These results demonstrate that surface roughness features like valley volume and voids significantly impact the apparent mechanical properties of piezoelectric films.

Keywords: nanoindentation; topography; piezoelectric

Citation: Bigerelle, M.; Lemesle, J.; Montagne, A.; Remiens, D. In-Situ Nanoindentation Surface Topography of Lead-Free Piezoelectric Thin Films. *Appl. Sci.* **2024**, *14*, 11849. https://doi.org/10.3390/app142411849

Academic Editors: Giorgio Biasiol and Evangelos Hristoforou

Received: 20 September 2024
Revised: 28 November 2024
Accepted: 12 December 2024
Published: 18 December 2024

1. Introduction

The selection of manufacturing parameters and processes has a direct impact on the surface morphologies and microstructures of materials, resulting in the generation of highly specific properties and functionalities [1–4]. In the work of Wang et al. [4], a correlation is demonstrated between larger grain structures and enhanced thermoelectric properties. Furthermore, it has been demonstrated that precise regulation of manufacturing process parameters facilitates recrystallization and size control of sub-nano regions, ultimately yielding materials with enhanced thermal conductivity and optimized performance [3]. More specifically, surface roughness is a critical characteristic that influences the response of many components in service. In the case of microelectromechanical systems (MEMS), their dynamic and electrostatic characteristics and their structural integrity partially depend on the surface roughness [5]. Surface roughness with positive skewness and sharp asperities (high kurtosis) is desirable to reduce adhesion. However, increasing surface roughness can cause contact loading to dominate adhesion forces, reducing the risk of permanent adhesion. It is important to find a compromise between reducing adhesion through sharp asperities and the structural reliability of the device. Numerous studies have focused on the influence of roughness on mechanical performance [6–8]. It is widely documented that an increase in roughness results in a significant discrepancy in the estimated values of hardness and

Young's modulus. This is due to the uncertainty inherent in the estimation of the contact area, which is more pronounced at shallow depth. Consequently, it is recommended to indent at a depth larger than the roughness, typically twenty times greater than the Ra parameter (ISO 14577-1 [9]). Alternatively, roughness can be reduced through polishing, although this may result in alterations to the mechanical properties [4]. For piezoelectric films, surface roughness plays an important role in the electromechanical behavior [10], e.g., the piezoelectric coefficient increases for lower roughness and more uniform surfaces [11].

When studying the mechanical properties of thin films, one of the main techniques used is nanoindentation, since it allows testing very small volumes of the material in an almost nondestructive way, providing the local intrinsic mechanical properties of the thin films [12].

Classically, atomic force microscopy (AFM) is used to measure the topography of surfaces after nanoindentation [13]. Some nanoindenters, notably Hysitron (Bruker, Billerica, MA, USA), include an in situ scanning probe microscope (SPM) to directly measure and study the indents [14]. In our work, the nanoindenter is directly used to measure the surface roughness of thin piezoelectric films.

The study of surface roughness always represents a complex subject because roughness parameters depend on their evaluation methods, therefore on the scale of measurement [15]. We have previously studied and proposed different methodologies to determine the most relevant roughness parameters that characterize the surface morphology regarding a particular function, property, or application [16,17]. This work firstly describes a methodology based on discriminant analysis to determine the most relevant roughness parameter. Then, we study which parameters provide a closer relationship with the mechanical properties by nanoindentation. Measuring the surface roughness in situ before and after nanoindentation tests with the nanoindentation probe offers the great advantage of obtaining topographic information of the sample at the same location of nanoindentation tests with a good precision. The interest of this work is to obtain direct information of the sample topography with the Berkovich indenter to distinguish between surfaces (thin lead-free piezoelectric films) and the combination with the mechanical properties.

The novelty and primary contribution of this work lies in combining surface characterization with mechanical testing to provide a more complete understanding of how surface roughness influences the performance of lead-free piezoelectric films in MEMS applications.

2. Materials and Methods

2.1. Piezoelectric Surfaces

For this study, four samples with lead-free piezoelectric thin films, composed of bismuth, sodium, and titanate (BNT), are studied. The films are deposited by radio frequency magnetron sputtering by varying thickness (220, 350, and 450 nm) on two types of substrate stacking layers, LNO/SiO_2/Si or LNO/Si (Table 1), where LNO ($LaNiO_3$) is the bottom electrode. These piezoelectric samples are here studied as they represent typical configurations of piezoelectric films used in MEMS, taking into account environmental regulation (lead removing).

BNTs are promising lead-free piezoelectric materials for a wide range of microelectronic applications: sensors, actuators, and energy storage [18–20]. The mechanical behavior of BNT piezoelectric materials has been extensively studied in the literature using local techniques such as indentation [21,22] and scratching [21,23]. These experimental techniques, which are particularly well suited to thin films and coatings, can be used to assess mechanical properties such as hardness and Young's modulus [22], residual stresses by measuring crack lengths [22], and the adhesion of the coating to the substrate [21,23]. In most cases, these evaluations require sample preparation with cutting and polishing, which can lead to a modification of the mechanical behavior [24]. In our study, we propose to observe the evolution of the apparent mechanical properties as a function of the native surface roughness, without any post-deposition modification.

Table 1. BNT film samples' characteristics [25].

Nomenclature	Substrate Stacking	Film Thickness (*t*) (nm)	Film Crystallization	Post-Annealing Treatment
BNTA (A)	LNO/Si	450	f-C	650 °C/1 h
BNTB (B)	LNO/Si	350	f-C	650 °C/1 h
BNTC (C)	LNO/SiO_2/Si	220	f-C	650 °C/1 h
BNTD (D)	LNO/SiO_2/Si	350	f-C	650 °C/1 h

f-C: Fully crystallized.

2.2. Nanoindentation Tests

The Hysitron Ti980 from Bruker (Billerica, MA, USA), equipped with a diamond Berkovich tip, was used to perform indentation tests. The tip area function was calibrated using a fused quartz reference sample, employing the Oliver and Pharr method [26]. The same methodology was employed for the processing of the experimental curves and the determination of the mechanical properties. Equations (1) and (2) are used to, respectively, determine the hardness H and the reduced Young's modulus E_r as defined in [26].

$$H = \frac{F_{max}}{A_c}, \tag{1}$$

where H is the hardness, F_{max} the maximum force applied, and A_c the projected contact area.

$$\frac{1}{E_r} = \frac{1-\nu_s^2}{E_s} + \frac{1-\nu_i^2}{E_i}, \tag{2}$$

where E_r is the reduced Young's modulus, E is the Young's modulus, and ν is the Poisson's ratio; subscripts s and i refer to sample and indenter, respectively.

Only the reduced modulus is reported here, since the Poisson's ratio of the BNT films is not reported elsewhere.

The analysis makes use of more than 400 reliable tests. The tests were conducted using the ultra-fast mapping mode (XPM mode) with arrays of 10 × 10 indents spaced by 1 µm. The arrays are spaced by 50 µM. The lateral move speed of the tip during the fast mapping was set to 10 µM/s, and the tip was maintained in contact with the surface at a setpoint of 1 µN. The maximum load applied was 250 µN, reached in 0.2 s. This was followed by a hold of 0.2 s, then an unloading of 0.2 s.

2.3. Topographical Measurements

The in situ topography measurements were performed by scanning probe microscopy (SPM) using the same tip as that used for nanoindentation, using the following settings: 256 × 256 pixels resolution, 3 µM × 3 µM images (point size of around 0.012 µM), 0.5 Hz scan rate, horizontal scan orientation, and 2 µN setpoint.

The 3D topographies of the four surfaces are presented in Figure 1. Roughness parameters from ISO 25178 [27] and EUR 15178N [28] were calculated on the measured topographical maps. The description of the parameters is given in Appendix A. The applied methodology and analysis to differentiate the surfaces are explained in Section 3.

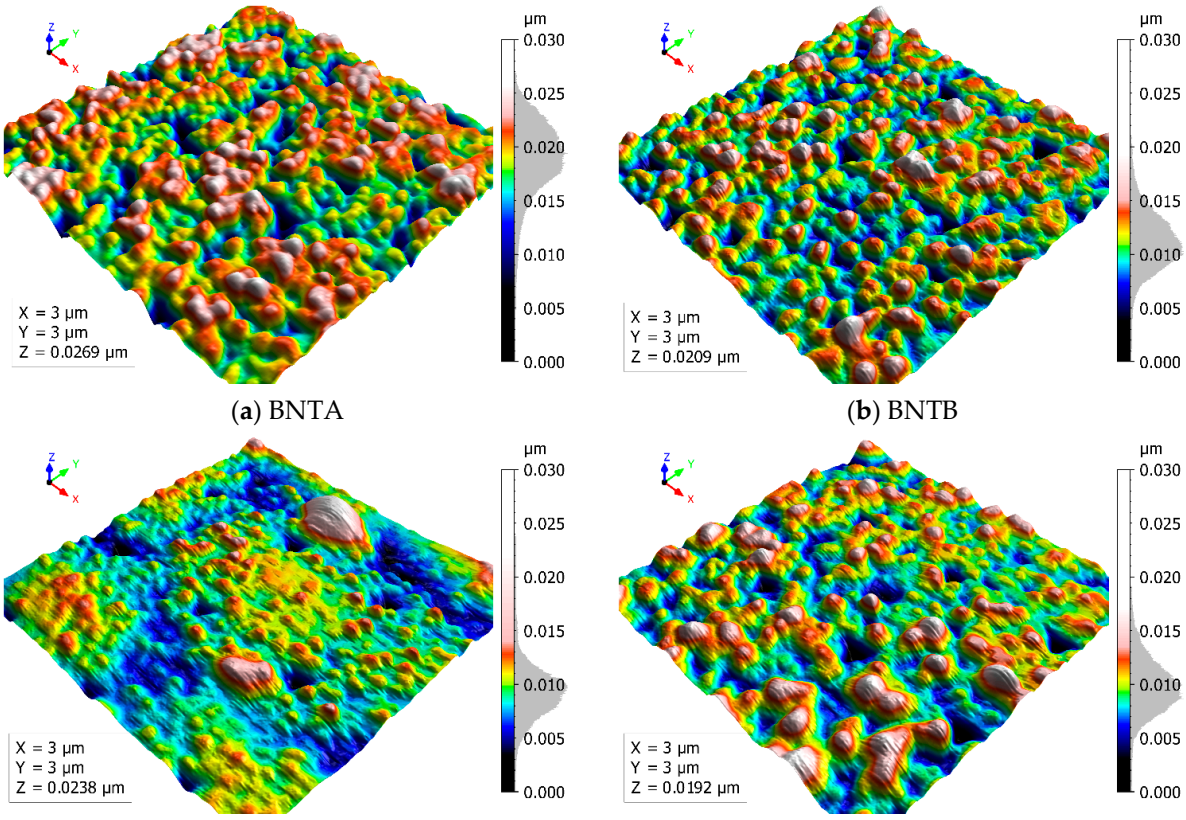

Figure 1. Initial 3D topography of the piezoelectric surfaces: 450 nm-LNO/Si (**a**), 350 nm-LNO/Si (**b**), 220 nm-LNO/SiO_2/Si (**c**), and 350 nm-LNO/SiO_2/Si (**d**). For each figure, the histogram corresponds to the distribution of the amplitudes of the surface points.

3. Results

3.1. Topography Analysis to Distinguish Between Surfaces

A discriminant analysis is used to determine which roughness parameter better distinguishes surfaces. In this analysis, each surface is assigned to one of four classes based on its roughness parameter: BNTA, BNTB, BNTC, and BNTD. The discriminant analysis consists of calculating the percentage of misclassified surfaces according to roughness parameters (e.g., Sa in Figure 2a), that is, the percentage of surfaces that do not correspond with the assigned classes [16]. To enhance the finesse of the analysis, we assess the probability density function of the parameters using a multidimensional Gaussian curve subsequent to the classification. The percentage of misclassified surfaces is then calculated by integration. This approach allows for the proposal of a probabilistic estimation of misclassified surfaces. A global indicator of the percentage of misclassified areas is obtained by summation of the misclassified areas per category. The principal interest of this kind of statistical analysis is to obtain a classification of different roughness parameters to better distinguish the studied surfaces, based on the misclassification percentage.

As a first step, the discriminant analysis described above was performed, selecting the parameter Sa (arithmetic mean height), as it is a standard measure in the domain of surface topography. This analysis makes it possible to determine if this parameter permits distinguishing the four surfaces. Figure 2a shows the histogram of the Sa mean values obtained through the bootstrap oversampling technique (1000 bootstraps) in accordance with a method developed by Bigerelle et al. [29]. The surface A presents a higher roughness (2.5 nm) than the surface C (1.7 nm), and the surfaces B and D are observed to have an equivalent level of roughness (2.0 nm). Regarding the Sa parameter, 25% of the surfaces were misclassified.

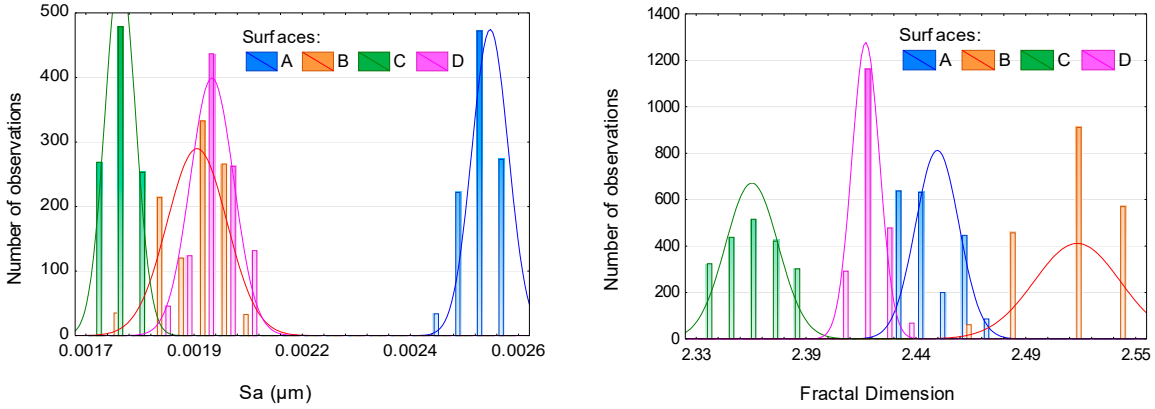

(**a**) Sa, whole scale, 25% misclassified

(**b**) Fractal dimension, whole scale, 2% misclassified

Figure 2. Roughness parameters analysis of the four surfaces (A, B, C, D) at the whole scale: Sa (**a**) and fractal dimension (**b**).

The roughness calculated here corresponds to the roughness of the bottom electrode (LNO) and the piezoelectric film (BNT). LNO films are deposited by sputtering at 450 °C followed by annealing at 700 °C to optimize electrical conductivity [30]. After this annealing treatment, a growth of the grains is observed that is not always homogeneous. The Sa values take into account these LNO grain size effects, which obviously affect the roughness of the heterostructure.

The same analysis was conducted using the fractal dimension, which yielded a misclassification rate of only 2%. The fractal dimensions of the surfaces are, respectively, 2.35, 2.41, 2.46, and 2.53 for C, D, A, and B (Figure 2b). These results suggest that the studied surfaces exhibit fractal characteristics, as evidenced by values exceeding 2. Additionally, the fractal dimensions indicate that the mechanisms underlying the formation of these surfaces are different and occur at multiple scales. It is noteworthy that surface B represents a perfect Brownian surface, indicated by its fractal dimension being closest to 2.5.

3.2. Multiscale Analysis

As a consequence of the fractal dimension results, a multiscale decomposition was performed on these surfaces. To this end, the surfaces were decomposed across multiple frequency ranges (from 2.00 nm to 2717.00 nm) through the application of high-pass filtering (to analyze the surface roughness), low-pass filtering (to analyze the surface waviness), and finally, band-pass filtering (to analyze a specific frequency [31]).

3.2.1. Multiscale Analysis of the Roughness Parameter Sa

The results for the multiscale and statistical analyses indicate that the surfaces exhibited greater discrimination when subjected to band-pass filtering at a cut-off length of 500 nm, resulting in a misclassification of 0.7% (Figure 3). At this length, the multiscale effect can be described in detail. Figure 4 illustrates the differences between the surfaces. This method allows the identification of the scale at which the decomposition becomes the most relevant, thereby establishing a characteristic scale in the complex representation of fractal roughness. Nevertheless, it can be assumed that the decomposition in band-pass filtering is a valuable method for morphologically observing the spatial description of the roughness. In that case, the role of altitude quantization cannot be used, as it is fundamentally dependent on the band-pass filter width. Though it can be asserted that the relationship A > D > B > C is relevant with respect to the amplitude of the characteristic roughness.

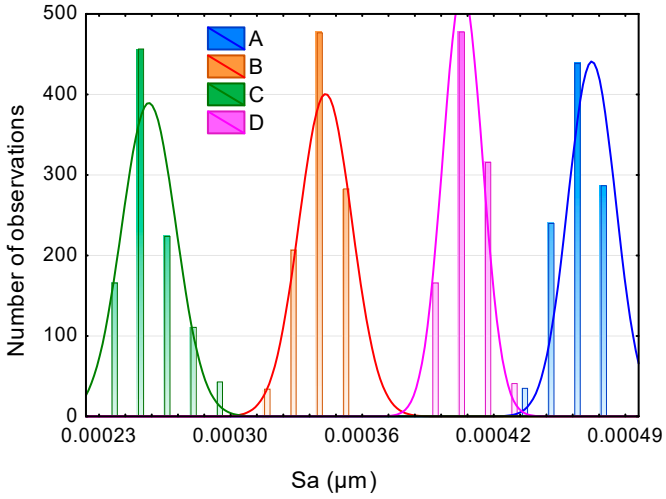

Figure 3. Histograms of the Sa parameter for the four surfaces, for band-pass filtering at 500 nm. For this filter and this scale, 0.7% of misclassification is obtained.

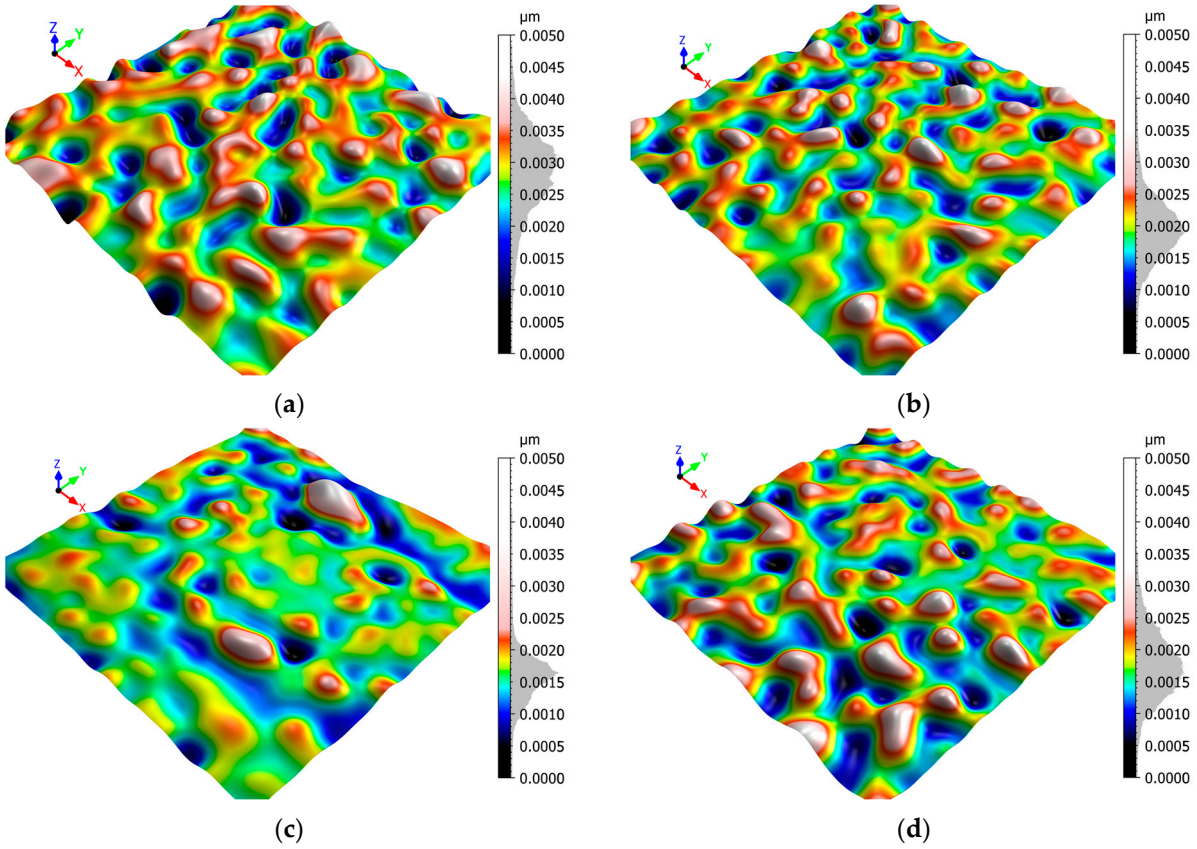

Figure 4. Best filtered (band-pass filtering, 500 nm) surfaces described by only the Sa roughness parameter. For each figure, the histogram corresponds to the distribution of the amplitudes of the surface points: (**a**) BNTA; (**b**) BNTB; (**c**) BNTC; and (**d**) BNTD.

3.2.2. Multiscale Analysis of All Roughness Parameters

A multiscale analysis was performed for 42 roughness parameters, in accordance with the standards set forth by the ISO 25178 [27] and EUR 15178N [28]. The analysis demonstrated that the Smr2 parameter is the most relevant one, exhibiting a 0.1% misclassification rate for the surfaces (Figure 5). The Smr2 parameter represents the percentage of the surface area occupied by valleys below a specified height threshold. Smr2 here discriminates the four surfaces (C < A < B < D) for a low-pass filter at 140 nm. This low-pass filtering removes

finer surface details in order to only highlight the broader features (large-scale valleys). This indicates that valleys are distinct at a scale superior to 140 nm. Figure 6 shows the topographic difference in the valleys, especially for the surface D, where the valleys are most prevalent.

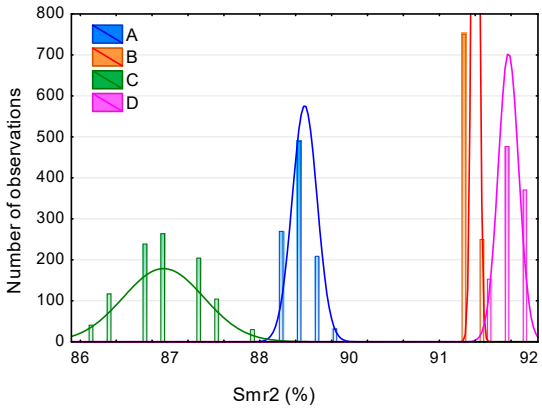

Figure 5. Histograms of the Smr2 parameter for the four surfaces, for a low-pass filtering at 140 nm. For this filter and this scale, 0.1% misclassification is obtained.

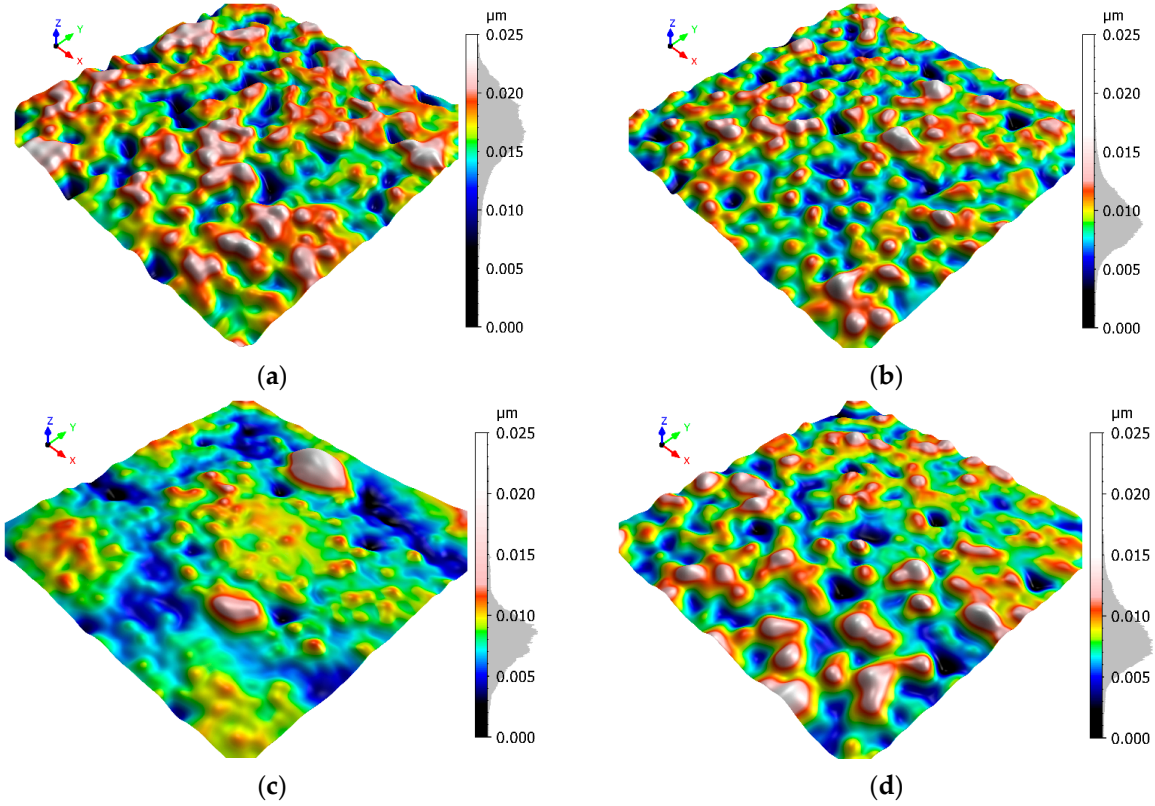

Figure 6. Best filtered (low-pass filter, 140 nm) surfaces described by only the Smr2 roughness parameter. For each figure, the histogram corresponds to the distribution of the amplitudes of the surface points: (**a**) BNTA; (**b**) BNTB; (**c**) BNTC; and (**d**) BNTD.

3.2.3. Multiscale Analysis: Two Parameters ($Sa^{s1,f1}$, $Sa^{s2,f2}$)

It may also be pertinent to consider whether the surface topography would be more accurately described by two morphology parameters rather than one [16]. First, the Sa value is calculated at different filtering frequencies and filtering types (high-pass, low-pass, and band-pass). Then, the percentage of misclassified surfaces assigned to a pair of Sa

roughness parameters noted ($Sa^{s1,f1}$, $Sa^{s2,f2}$) is calculated, where s represents the filtering type and f the size of the filtering cut-off length. By testing all two-by-two combinations of the different Sa, the relevance of these couples is classified by sorting them by increasing the order of misclassified surfaces. The optimal pair identified is ($Sa^{\text{No Filter, whole scale}}$, $Sa^{\text{high-pass, 277nm}}$) with 10^{-11}% misclassified surfaces (Figure 7). The very low integral density probability values, such as 10^{-11}, serve as measures of discrimination distance rather than conventional probabilities. These values highlight the distinct separation between clusters, underscoring the discriminative power of the parameters. Therefore, the four studied surfaces can be described in a relevant way by a combination of the Sa parameter (no filter, full scale) and the Sa parameter at a finer scale (277 nm), including a nuance on the roughness amplitude at this spatial scale.

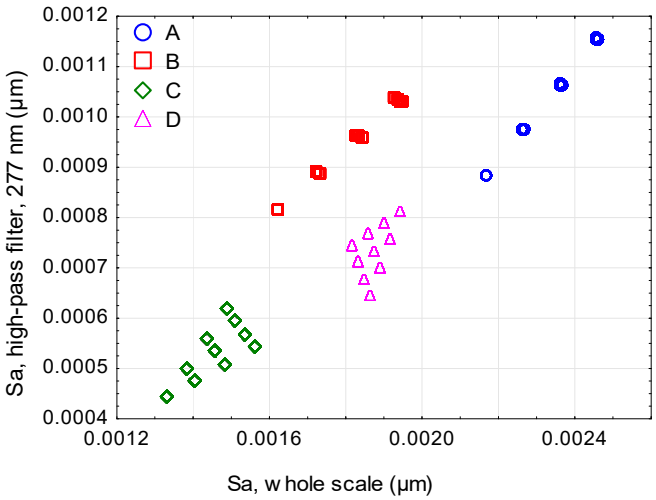

Figure 7. Sa for a high-pass filter at 277 nm versus Sa at the whole scale (no filter); 10^{-11}% misclassified.

The graph visualization ($Sa^{\text{No Filter, whole scale}}$, $Sa^{\text{high-pass, 277nm}}$) is replete with information (Figure 7). As previously shown for the Sa parameter without filtering, the surfaces B and D have similar Sa values, which diverge from those observed for A and C. However, surfaces B and D display a more pronounced disparity for $Sa^{\text{high-pass, 277nm}}$, with surface B exhibiting an approximate 0.2 nm higher value. This observation tends to support the fact that surface B has a higher fractal dimension (Figure 2b), approaching the Brownian surface (fractal dimension equal to 2.5). Moreover, the surfaces A, C, and D have values ($Sa^{\text{No Filter, whole scale}}$, $Sa^{\text{high pass, 277nm}}$) aligned on the same line of equation $Sa^{\text{No Filter}} = 0.5 \times Sa^{\text{high pass, 277nm}}$, showing a behavior of similar scale, different from the surface B.

3.2.4. Multiscale Analysis: Two Parameters ($Spc^{\text{No Filter}}$, $Vvc^{\text{No Filter}}$) and Best Couple of Parameters at Whole Scale

The multiscale two-parameter analysis was conducted for additional parameter combinations without the application of any filter. The parameter pair ($Spc^{\text{No Filter}}$, $Vvc^{\text{No Filter}}$) yielded the most relevant couple for discriminating surfaces, with a misclassified percentage of approximately 10^{-31}% (Figure 8). The surfaces C, D, and A are discriminated by the volume of roughness, with surface A exhibiting the greatest roughness, followed by surfaces D and C, respectively. The surface B is distinguished from the surface D by the curvature of the peaks, which are less curved in surface B than in surface D.

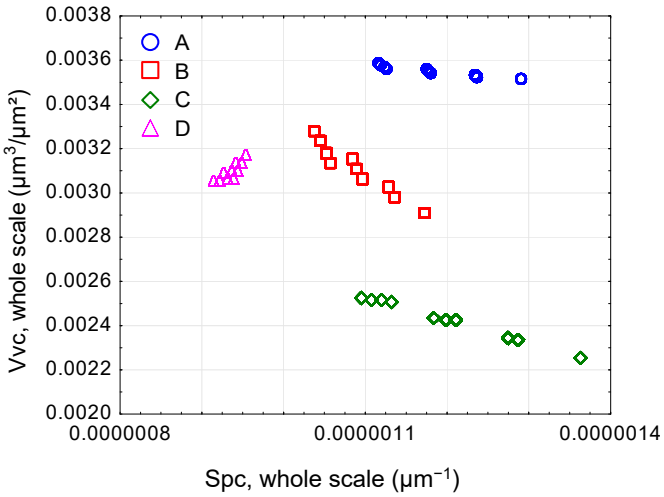

Figure 8. Spc versus Vvc, at the whole scale (no filter); 1.9×10^{-31}% misclassified.

3.3. Relationship Between Mechanical Properties by Nanoindentation and Roughness Parameters

The surface topography of the four surfaces under investigation reflects the different conditions of the surface production processes. It is thus appropriate to analyze the potential relationships between the mechanical properties (hardness and elastic modulus) of the material and the surface topography [32]. For this, we will examine the hypothesis of a linear relationship (Equation (3)) between a mechanical property of the surface (hardness or elastic modulus) and a morphological property of the surface (roughness parameter obtained with a given filter), i.e., the shape.

$$m_i = a_{i,j,p,q}\, r_j^{s_p,f_q} + b_{i,j,p,q}, \tag{3}$$

where the variables are defined as follows:

- $m_i, i \in \{1..I\}$ is a mechanical property of the surface (m_1 is the hardness in GPa and m_2 is the reduced elastic modulus in GPa);
- $r_j^{s_p,f_q}$ is the r_j roughness parameter computed with a s_p filter at a cut-off length f_q with $j \in \{1..J\},\ p \in \{1..P\}, q \in \{1..Q\}$;
- $a_{i,j,p,q}$ et $b_{i,j,p,q}$ are two constants.

To assess the quality of the proposed model, the coefficients $a_{i,j,p,q}$ and $b_{i,j,p,q}$ are calculated using the least square method, and the correlation coefficient noted $R^2\left(m_i, r_j^{s_p,f_q}\right)$ is calculated. By performing all possible permutations of the indices $\{j, p, q\}$ for a mechanical property m_i and by solving Equation (3) for each element containing $J \times P \times Q$, we will obtain the values of $R_i{}^2\left(m_i, r_j^{s_p,f_q}\right)$ for the m_i mechanical property.

Figure 9 represents the values of $R^2\left(H, r_j^{s_p,f_q}\right)$ and $R^2\left(E, r_j^{s_p,f_q}\right)$ as a function of the order of classification, which is related to the tested roughness parameters. The first position in the 'Order of classification' axis corresponds to the roughness parameters exhibiting the best correlation (highest R^2) with the mechanical parameters, specifically hardness (blue curve, Figure 9) and Young's modulus (red curve, Figure 9).

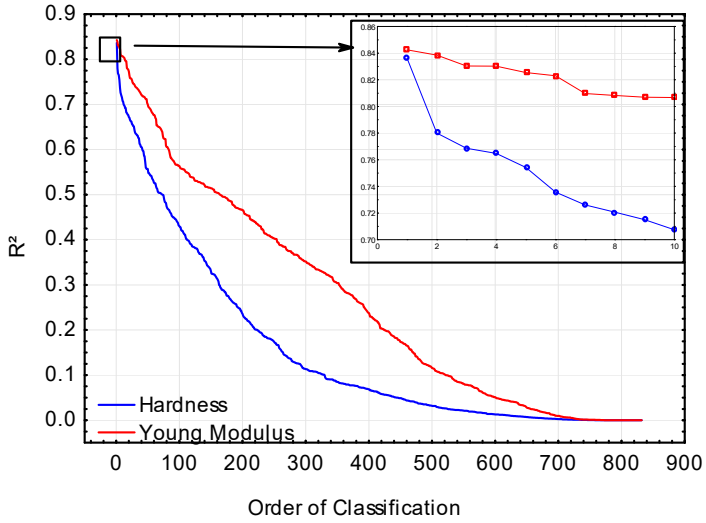

Figure 9. R^2 values versus classification order of the roughness parameters according to the mechanical properties.

In order to have a robust quantification of experimental error, ensuring that observed differences in mechanical properties are statistically significant and not merely due to experimental variation. The mean hardness and modulus values are calculated using a bootstrapping method over the 100 nanoindentation measurements for each surface.

The roughness parameters that exhibited the strongest correlation were Smr2 with a low-pass filtering at 500 nm for the hardness ($R^{2(H,r_j^{low-pass,\ 500\ nm})} = 0.82$) and Vvc with a low-pass filtering at 2 nm for the reduced elastic modulus ($R^{2(E,r_j^{low-pass,\ 2\ nm})} = 0.84$). Figure 10 shows the correlation between these two parameters at their relevant spatial scales. Each data point in Figure 10 represents the bootstrap mean of two considered parameters, showing the variance across surfaces. Although the clusters appear discrete due to the limited number of measurements, Gaussian smoothing densities provide a continuous classification within clusters, supporting the linear relationship observed.

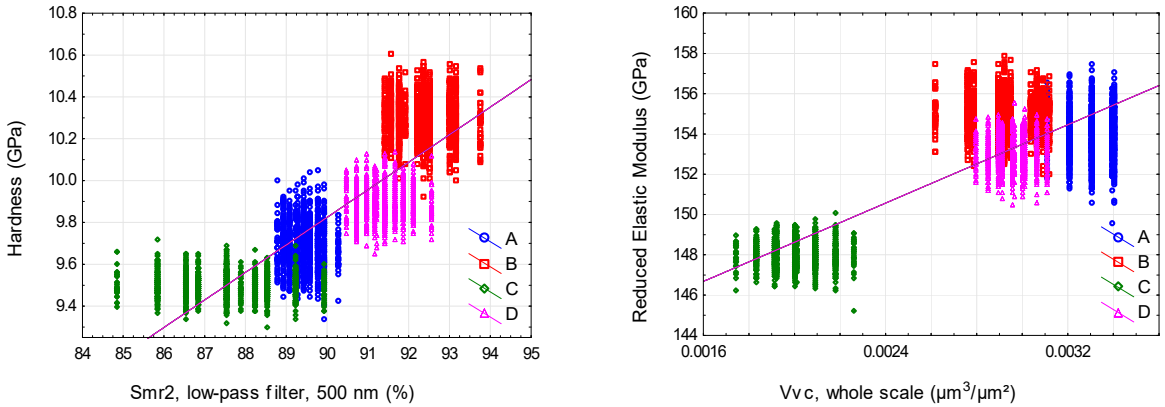

(**a**) Hardness versus Smr2 (low-pass filter, 500 nm), R² = 0.82

(**b**) Reduced Elastic Modulus versus Vvc (low-pass filter, 2 nm), R² = 0.84

Figure 10. Relation between mechanical properties obtained by nanoindentation and roughness parameters. The best relation ($R^2 = 0.82$) between the hardness and the roughness parameter Smr2 is obtained for a low-pass filtering at 500 nm (**a**). The best relation ($R^2 = 0.84$) between the reduced elastic modulus and the roughness parameter Vvc at the whole scale (equivalent to low-pass/2 nm) (**b**).

It should be noted that the hardness and the modulus show small differences between the four surfaces, about 1 GPa for the hardness and 10 GPa for the modulus (Figure 11).

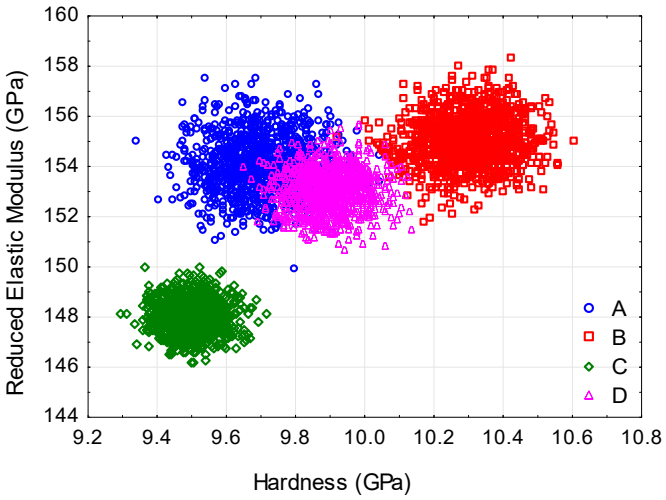

Figure 11. Reduced elastic modulus versus hardness.

These results put in evidence some findings. With regard to the hardness, it was observed that as the valley regime assumes greater significance for cut-off lengths exceeding 500 nm (low-pass filter), the hardness values tend to increase. The surface designated as B (Brownian surface of fractal dimension 2.5) exhibited a higher hardness value. Thus, it seems that the fractal nature of the surface is responsible for the observed increase in hardness, which is attributed to an increase in the proportion of large valleys. With regard to the elastic modulus, there is an observable increase in relation to the void volume of the roughness core, Vvc. Hence, suggesting that the presence of voids related to the surface roughness produces an increment in the stiffness of the surfaces.

It can be noted that while the methodology reliably distinguishes between the four samples in this study, the reproducibility of these results may vary with different deposition conditions or material compositions. As such, further studies could extend this analysis across a broader range of samples and processing techniques to validate the generality of these correlations.

4. Conclusions

The methodology proposed in this study is designed to identify meaningful roughness parameters that can capture complex topographic features that influence mechanical properties (hardness and reduced elastic modulus). This methodology is based on a structured discriminant analysis associated with a bootstrapping technique and the multiscale study of the surfaces.

The study demonstrates that the surfaces of piezoelectric thin films exhibit fractal characteristics, with the fractal dimension providing better surface distinction compared to traditional roughness parameters. For instance, the Sa parameter misclassified 25% of surfaces, whereas the fractal dimension reduced misclassification to 2%. Surfaces with higher fractal dimensions, particularly those close to a Brownian surface (fractal dimension ≈ 2.5), exhibited higher hardness, especially when large valleys dominated the topography. A multiscale roughness analysis using various filters (high-pass, low-pass, and band-pass) further refined the surface distinctions. Band-pass filtering at a 500 nm cut-off for the Sa parameter reduced misclassification to 0.7%, and low-pass filtering at 140 nm for the Smr2 parameter brought it down to just 0.1%.

Additionally, the study identified a significant correlation between mechanical properties and surface roughness. The valley regime, represented by the Smr2 parameter, exhibited the strongest correlation with hardness ($R^2 = 0.82$), particularly with low-pass

filtering at 500 nm, where larger valleys were linked to increased hardness. Similarly, the void volume of the roughness core (Vvc) exhibited a strong correlation with the reduced elastic modulus (R^2 = 0.84), indicating that surface voids contribute to increased stiffness. These results highlight the significance of specific roughness characteristics in influencing the mechanical behavior of piezoelectric films.

Despite the limited number of samples, representing typical configurations of lead-free piezoelectric films used in MEMS and covering a significant range of surface properties, the results are robust, with strong correlations observed between roughness parameters (Smr2 and Vvc) and mechanical properties. These findings provide a solid foundation for future studies with more samples, which could further validate and expand the conclusions.

Author Contributions: Methodology, M.B.; software, M.B.; validation, M.B., J.L., and A.M.; resources, D.R.; writing—original draft preparation, M.B., J.L., and A.M.; writing—review and editing, M.B., J.L., and A.M.; supervision, M.B. and D.R. All authors have read and agreed to the published version of the manuscript.

Funding: This work was carried out within the framework of the Junior Professor Chair MesuRufo, cofounded by ANR, UPHF, and CNRS.

Institutional Review Board Statement: Not applicable.

Informed Consent Statement: Not applicable.

Data Availability Statement: Data are contained within the article.

Conflicts of Interest: Author Julie Lemesle was employed by the company U.R Concept. The remaining authors declare that the research was conducted in the absence of any commercial or financial relationships that could be construed as a potential conflict of interest.

Appendix A

Roughness parameters of the topographic maps according to the standards ISO 25178 and EUR 15178N, calculated for different categories listed below:

- Amplitudes parameters: Sq (root-mean-square height), Ssk (skewness), Sku (kurtosis), Sp (maximum peak height), Sv (maximum pit height), Sz (maximum height), Sa (arithmetic mean height);
- Functional parameters (area): Smr (areal material ratio), Smc (inverse areal material ratio), Sxp (extreme peak height);
- Hybrid parameters: Sdq (root-mean-square gradient, Sdr (developed interfacial area ratio), Ssc (arithmetic mean summit curvature, EUR 15178N), Sfd (fractal dimension of the surface, EUR 15178N);
- Functional parameters (volume): Vm (material volume), Vv (void volume), Vmp (peak material volume), Vmc (core material volume), Vvc (core void volume), Vvv (pit void volume), Sk (core roughness depth), Spk (reduced summit height), Svk (reduced valley depth), Smr1 (upper bearing area), Smr2 (lower bearing area), Spq (plateau root-mean-square roughness), Svq (valley root-mean-square roughness), Smq (material ratio at plateau-to-valley transition), Sbi (surface bearing index, EUR 15178N), Sci (core fluid retention index, EUR 15178N), Svi (valley fluid retention index, EUR 15178N);
- Feature parameters: Spd (density of peaks), Spc (arithmetic mean peak curvature), S10z (ten-point height), S5p (five-point peak height), S5v (five-point pit height), Sda (mean dale area), Sha (mean hill area), Sdv (mean dale volume), Shv (mean hill volume), Svd (density of pits), Svc (arithmetic mean pit curvature).

References

1. Ding, W.; Xu, W.; Dong, Z.; Liu, Y.; Wang, Q.; Shiotani, T. Piezoelectric Properties and Microstructure of Ceramicrete-Based Piezoelectric Composites. *Ceram. Int.* **2021**, *47*, 29681–29687. [CrossRef]
2. Kathavate, V.S.; Prasad, K.E.; Kiran, M.S.R.N.; Zhu, Y. Mechanical Characterization of Piezoelectric Materials: A Perspective on Deformation Behavior across Different Microstructural Length Scales. *J. Appl. Phys.* **2022**, *132*, 121103. [CrossRef]

3. Liu, W.-D.; Yin, L.-C.; Li, L.; Yang, Q.; Wang, D.-Z.; Li, M.; Shi, X.-L.; Liu, Q.; Bai, Y.; Gentle, I.; et al. Grain Boundary Re-Crystallization and Sub-Nano Regions Leading to High Plateau Figure of Merit for Bi2Te3 Nanoflakes. *Energy Environ. Sci.* **2023**, *16*, 5123–5135. [CrossRef]
4. Wang, D.-Z.; Liu, W.-D.; Mao, Y.; Li, S.; Yin, L.-C.; Wu, H.; Li, M.; Wang, Y.; Shi, X.-L.; Yang, X.; et al. Decoupling Carrier-Phonon Scattering Boosts the Thermoelectric Performance of n-Type GeTe-Based Materials. *J. Am. Chem. Soc.* **2024**, *146*, 1681–1689. [CrossRef]
5. Tayebi, N.; Polycarpou, A.A. Adhesion and Contact Modeling and Experiments in Microelectromechanical Systems Including Roughness Effects. *Microsyst. Technol.* **2006**, *12*, 854–869. [CrossRef]
6. Bobji, M.S.; Biswas, S.K. Estimation of Hardness by Nanoindentation of Rough Surfaces. *J. Mater. Res.* **1998**, *13*, 3227–3233. [CrossRef]
7. Bobji, M.S.; Biswas, S.K. Deconvolution of Hardness from Data Obtained from Nanoindentation of Rough Surfaces. *J. Mater. Res.* **1999**, *14*, 2259–2268. [CrossRef]
8. Qasmi, M.; Delobelle, P. Influence of the Average Roughness *R*Ms on the Precision of the Young's Modulus and Hardness Determination Using Nanoindentation Technique with a Berkovich Indenter. *Surf. Coat. Technol.* **2006**, *201*, 1191–1199. [CrossRef]
9. *ISO 14577-1*; Metallic Materials—Instrumented Indentation Test for Hardness and Materials Parameters—Part 1: Test Method. The International Organization for Standardization: Geneva, Switzerland, 2015.
10. Nawaz, H.; Masood, M.U.; Saleem, M.M.; Iqbal, J.; Zubair, M. Surface Roughness Effects on Electromechanical Performance of RF-MEMS Capacitive Switches. *Microelectron. Reliab.* **2020**, *104*, 113544. [CrossRef]
11. Taleb, S.; Badillo-Ávila, M.A.; Acuautla, M. Fabrication of Poly (Vinylidene Fluoride) Films by Ultrasonic Spray Coating; Uniformity and Piezoelectric Properties. *Mater. Des.* **2021**, *212*, 110273. [CrossRef]
12. Pharr, G.M.; Oliver, W.C. Measurement of Thin Film Mechanical Properties Using Nanoindentation. *MRS Bull.* **1992**, *17*, 28–33. [CrossRef]
13. Cech, V.; Lasota, T.; Palesch, E.; Lukes, J. The Critical Influence of Surface Topography on Nanoindentation Measurements of A-SiC:H Films. *Surf. Coat. Technol.* **2015**, *261*, 114–121. [CrossRef]
14. Smith, C.M.; Jiang, D.; Gong, J.; Yin, L. Determination of the Mechanical Behavior of Lithium Disilicate Glass Ceramics by Nanoindentation & Scanning Probe Microscopy. *Mater. Chem. Phys.* **2014**, *148*, 1036–1044. [CrossRef]
15. Van Gorp, A.; Bigerelle, M.; Grellier, A.; Iost, A.; Najjar, D. A Multi-Scale Approach of Roughness Measurements: Evaluation of the Relevant Scale. *Mater. Sci. Eng. C* **2007**, *27*, 1434–1438. [CrossRef]
16. Bigerelle, M.; Najjar, D.; Mathia, T.; Iost, A.; Coorevits, T.; Anselme, K. An Expert System to Characterise the Surfaces Morphological Properties According to Their Tribological Functionalities: The Relevance of a Pair of Roughness Parameters. *Tribol. Int.* **2013**, *59*, 190–202. [CrossRef]
17. Lemesle, J.; Robache, F.; Le Goic, G.; Mansouri, A.; Brown, C.A.; Bigerelle, M. Surface Reflectance: An Optical Method for Multiscale Curvature Characterization of Wear on Ceramic–Metal Composites. *Materials* **2020**, *13*, 1024. [CrossRef]
18. Li, L.; Fan, P.; Wang, M.; Takesue, N.; Salamon, D.; Vtyurin, A.N.; Zhang, Y.; Tan, H.; Nan, B.; Lu, Y.; et al. Review of Lead-Free Bi-Based Dielectric Ceramics for Energy-Storage Applications. *J. Phys. Appl. Phys.* **2021**, *54*, 293001. [CrossRef]
19. Zhu, W.; Shen, Z.-Y.; Deng, W.; Li, K.; Luo, W.; Song, F.; Zeng, X.; Wang, Z.; Li, Y. A Review: (Bi,Na)TiO3 (BNT)-Based Energy Storage Ceramics. *J. Materiomics* **2024**, *10*, 86–123. [CrossRef]
20. Supriya, S. A Review on Lead-Free-Bi0.5Na0.5TiO3 Based Ceramics and Films: Dielectric, Piezoelectric, Ferroelectric and Energy Storage Performance. *J. Inorg. Organomet. Polym. Mater.* **2022**, *32*, 3659–3676. [CrossRef]
21. Kusukawa, K.; Xu, F. Evaluation of Interfacial Strength of Bnt Films Hydrothermally Deposited on Titanium Substrates. *Int. J. Mod. Phys. B* **2010**, *24*, 3053–3058. [CrossRef]
22. Ayrikyan, A.; Prach, O.; Khansur, N.H.; Keller, S.; Yasui, S.; Itoh, M.; Sakata, O.; Durst, K.; Webber, K.G. Investigation of Residual Stress in Lead-Free BNT-Based Ceramic/Ceramic Composites. *Acta Mater.* **2018**, *148*, 432–441. [CrossRef]
23. Xu, F.C.; Kusukawa, K. Adhesion Assessment of BNT Films on Titanium Substrates Using a Scratch Test. *Adv. Mater. Res.* **2014**, *875–877*, 584–587. [CrossRef]
24. Liu, Y.; Ngan, A.H.W. Depth Dependence of Hardness in Copper Single Crystals Measured by Nanoindentation. *Scr. Mater.* **2001**, *44*, 237–241. [CrossRef]
25. Kossman, S.; Hamieh, A.; Ponchel, F.; Rémiens, D.; Bigerelle, M. Electromechanical Properties of Sodium Bismuth Titanate Thin Films. *Thin Solid Films* **2022**, *759*, 139459. [CrossRef]
26. Oliver, W.C.; Pharr, G.M. An Improved Technique for Determining Hardness and Elastic Modulus Using Load and Displacement Sensing Indentation Experiments. *J. Mater. Res.* **1992**, *7*, 1564–1583. [CrossRef]
27. *ISO 25178-2*; Geometrical Product Specifications (GPS)—Surface Texture: Areal—Part 2: Terms, Definitions and Surface Texture Parameters. International Organization for Standardization: Geneva, Switzerland, 2012.
28. Stout, K.J.; Blunt, L.; Dong, W.P.; Mainsah, E.; Luo, N.; Mathia, T.; Sullivan, P.J.; Zahouani, H. *BCR Report EUR 15178N—The Development of Methods for the Characterisation of Roughness in Three Dimensions*; European Commission: Brusels, Belgium, 1993.
29. Bigerelle, M.; Gautier, A.; Iost, A. Roughness Characteristic Length Scales of Micro-Machined Surfaces: A Multi-Scale Modelling. *Sens. Actuators B Chem.* **2007**, *126*, 126–137. [CrossRef]

30. Sama, N.; Herdier, R.; Jenkins, D.; Soyer, C.; Remiens, D.; Detalle, M.; Bouregba, R. On the Influence of the Top and Bottom Electrodes—A Comparative Study between Pt and LNO Electrodes for PZT Thin Films. *J. Cryst. Growth* **2008**, *310*, 3299–3302. [CrossRef]
31. Berglund, J.; Agunwamba, C.; Powers, B.; Brown, C.; Rosén, B.-G. On Discovering Relevant Scales in Surface Roughness Measurement-An Evaluation of a Band-Pass Method. *Scanning* **2010**, *32*, 244–249. [CrossRef]
32. Marteau, J.; Bigerelle, M. Relation between Surface Hardening and Roughness Induced by Ultrasonic Shot Peening. *Tribol. Int.* **2015**, *83*, 105–113. [CrossRef]